# Characterization of the optical properties of an infrared blocked impurity band detector

S. I. Woods,[1,*] S. G. Kaplan,[1] T. M. Jung,[2] and A. C. Carter[3]

[1]Optical Technology Division, National Institute of Standards and Technology, 100 Bureau Drive, MS 8441, Gaithersburg, Maryland 20899, USA

[2]Jung Research and Development Corp., Washington, DC 20009, USA

[3]Booz Allen Hamilton Inc., Arlington, Virginia 22203, USA

*Corresponding author: solomon.woods@nist.gov

Received 28 February 2011; revised 3 June 2011; accepted 28 June 2011; posted 14 July 2011 (Doc. ID 143249); published 16 August 2011

Si:As blocked impurity band detectors have been partially deprocessed and measured by Fourier transform spectroscopy to determine their transmittance and reflectance at cryogenic temperatures over the wavelength range 2 $\mu$m to 40 $\mu$m. A method is presented by which the propagation constants can be extracted from an inversion of the transmittance and reflectance data. The effective propagation constants for the active layer from 2 $\mu$m to 20 $\mu$m were calculated as well as the absorption cross section of arsenic in silicon, which agrees well with previous results from the literature. The infrared absorptance of the full detector was determined, and the analytical method also provides an estimate of absorption in the active layer alone. Infrared absorptance of the active layer is compared to the quantum yield measured by photoelectric means on similar detectors. The optical methods outlined here, in conjunction with standard electronic measurements, could be used to predict the performance of such detectors from measurements of the blanket films from which they are to be fabricated. 

*OCIS codes:* 040.3060, 040.5160, 120.4530, 160.1890, 300.6340.

## 1. Introduction

Blocked impurity band (BIB) devices based upon doped semiconductors exhibit excellent properties for detection and imaging in the infrared (IR) [1–3]. BIB detectors are already of crucial importance for optical calibration and astronomical measurements in the wavelength range from 2 $\mu$m to 30 $\mu$m, and they have the potential for measurements in the far IR out to 1 mm [4]. The National Institute of Standards and Technology (NIST) uses BIB detectors as the basis for transfer of low-power IR standards [5–7] and BIB arrays are employed on instruments of ground and space-based telescope systems, including the Keck, Spitzer, and James Webb telescopes. BIB detectors must in general be operated at cryogenic temperatures but offer low noise in addition to high responsivity, speed, linearity, and spatial uniformity [8].

Silicon doped with arsenic (Si:As) is the most common IR-active material used in BIB detectors and for common doping levels offers responsivity from 2 $\mu$m to 30 $\mu$m with demonstrated quantum yield as high as 60%. A number of papers have modeled the electronic performance of BIB detectors [9,10]. Despite the scientific importance of these detectors, however, few studies have attempted to measure the optical properties of the materials used in BIB detector fabrication and correlate these properties with the performance of working detectors [11]. Measurements of the optical properties of Si:As provide complementary information to electronic measurements, and taken together with electronic data could be used to predict the performance of BIB detectors based on measurements of the thin film stack from which they are to be fabricated.

0003-6935/11/244824-10$15.00/0

We have measured by IR Fourier transform spectroscopy (FTS) the low temperature transmittance and reflectance of partially deprocessed Si:As BIB detectors and developed a method to extract basic optical constants from the data in the incoherent limit. The complex propagation constant and the absorption cross section of Si:As have been computed, and the projected absorptance of a BIB detector using this material has also been estimated. Our results for the low temperature absorption cross section of Si:As agree well with previous data in the literature, bolstering the validity of our optical measurements. The absorptance for the BIB detector has been calculated in two ways and agrees well with an estimate made using a coherent model, which validates our use of the incoherent limit in most of the analysis. The results of the optical measurements have been compared to quantum yield results determined by the manufacturer of the BIBs from photoelectric measurements on detectors from the same fabrication lot. The ratio of the quantum yield to absorptance provides an empirical spectral curve related to the product of collection efficiency and detector gain.

## 2. Experimental Procedures

The samples studied were backside-illuminated Si:As BIB detectors, employing nominally transparent contacts on either side of the IR-active layer (AL). A schematic of the detector geometry is shown in Fig. 1. Photons travel through about 350 $\mu$m of undoped Si substrate and pass through the buried transparent contact before reaching the IR-AL, which is composed of approximately 15 $\mu$m of Si:As with As concentration approximately $1 \times 10^{18}$ cm$^{-3}$. For operation as a photodetector, a reverse bias is applied between the front and buried contacts. Absorbed photons generate photo-electrons as well as ionized arsenic sites from which the electrons were ejected. The photo-electrons are swept by the bias voltage to the front contact and the positive ionized donor sites hop to the buried contact, which constitutes the detector response. The buried contact and front contact are made by degenerate doping of Si with Sb and As, respectively. The blocking layer, made from 3 $\mu$m of undoped Si, impedes the ability of the positive charges from ionized donor sites to hop between electrodes and be registered as dark current. Photons

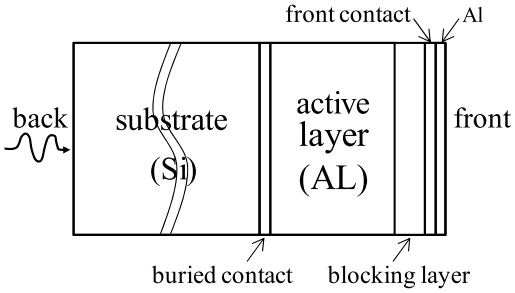


Fig. 1. Schematic of the backside-illuminated BIB detectors measured in this study. The silicon substrate is about 350 $\mu$m thick and the Si:As IR-AL is about 15 $\mu$m thick.

that are transmitted through the AL are effectively reflected by the aluminum on the front surface, giving a high probability the photons will have another chance to be absorbed in the IR-AL.

For the optical measurements, the BIB samples were partially deprocessed to allow transmission of photons entirely through the devices. An aluminum etch was used to remove the front metallization and a buffered oxide etch was used to remove silicon dioxide between the metallization and front transparent contact. The front surface was then mechanically polished through the blocking layer, so the AL would become the exposed surface. After etching, but before polishing, the measurement sample was divided into three subsamples, one to be used for secondary ion mass spectroscopy (SIMS) to determine the concentration profile of the BIB devices, one to be used for profilometer measurements to monitor how much material was polished away, and one for the FTS measurements.

SIMS measurement was performed by Evans Analytical Group using a 14.5 keV Cs primary beam, and the As concentration was calibrated against a silicon standard [12]. Sputtering of the sample was completed to a depth of 18 $\mu$m, capturing information on all the layers above the silicon substrate. Photocurrent measurements on undamaged BIB devices from the same fabrication lot were made by the manufacturer (originally a unit of Rockwell Science Center, now DRS Sensors & Targeting Systems) and verified in our laboratory [12]. The spectral quantum yield curve was determined by the manufacturer, and verification of the quantum yield at NIST was accomplished using a monochromator measurement with scaling and spectral weighting determined by comparison with the response of an absolute cryogenic radiometer standard [5].

Optical measurements were made using a Bomem DA FTIR spectrometer with the samples held at temperature (typically near 12 K or 300 K) in an Oxford CF1104 optical cryostat [12]. Samples were diced to 12.7 mm square size and placed on a mount with a 7 mm aperture. An aperture of 2.5 mm or 3.5 mm was used in the $f/4$ light source from the spectrometer, and steps were taken to ensure there was no clipping of the beam before it reached the detector. Transmittance measurements were made with a three-position stage in the cryostat, which allowed three separate sample locations to be repeatedly placed in front of the beam for each measurement condition. The sample on its mount with the 7 mm aperture was placed in the first stage position, an identical empty mount was placed in the second position, and the third position was left entirely blank (leaving a 25.4 mm through-hole). Sample transmittance was normalized by transmittance through the empty identical mount, and transmittance through the blank position was used to verify that the source beam could be reliably centered through the 7 mm aperture of the mounts. For the reflectance measurements, two sample stage positions were used, one

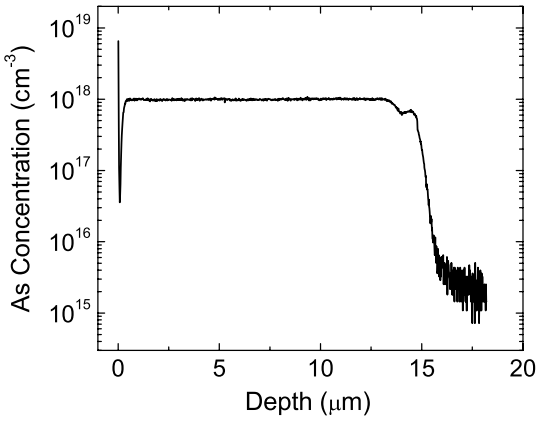


Fig. 2. SIMS data for a partially deprocessed BIB detector used for FTS measurements. Depth is measured from the frontside of the detector, which is the surface of the AL exposed by deprocessing. The AL arsenic doping is very close to $1.0 \times 10^{18}\ \mathrm{cm}^{-3}$.

holding the sample on its mount with the 7 mm aperture and the other holding a gold-coated mirror with approximately 99% reflectance over the measured wavelengths. The reflectance measurements were made using a commercial reflectance accessory, which allowed the reflected beam from the sample or reference to be steered to the detector.

Measurements were made over two wavelength ranges, the shorter wavelengths from 2 $\mu$m to 20 $\mu$m and the longer wavelengths from 15 $\mu$m to 40 $\mu$m. In both cases, deuterated triglycine sulfide detectors were used, with a KBr window in the short wavelength case and a polyethylene window for the long wavelength detector. In the short wavelength case, a KBr beamsplitter was used in the Fourier transform (FT) spectrometer and KCl windows were used in the cryostat. In the long wavelength case, a 3 $\mu$m Mylar film beamsplitter was used in the FT spectrometer and KRS-5 windows in the cryostat. For the cold measurements, background spectra with the source off were taken so the thermal signal from the experimental optics could be subtracted from the source-on spectra. Spectra were taken at room temperature and at temperatures between 4.2 K and 12 K. The spectral resolution of the measurements at shorter wavelengths for transmittance was $4\ \mathrm{cm}^{-1}$ and for all other measurements was relaxed to $8\ \mathrm{cm}^{-1}$.

### 3. Experimental Results

SIMS data shows that the arsenic concentration in silicon for the samples is very near $10^{18}\ \mathrm{cm}^{-3}$ in the AL and that the surface polishing of the FTS sample reached the desired depth. The SIMS profile for arsenic, with depth measured from the frontside surface of the AL, is shown in Fig. 2. The arsenic-doped layer is approximately 15 $\mu$m deep and from 1 $\mu$m to 13 $\mu$m its arsenic concentration averages $9.94 \times 10^{17}\ \mathrm{cm}^{-3}$ (standard deviation $2.21 \times 10^{16}\ \mathrm{cm}^{-3}$). The high arsenic level at the surface is probably a SIMS artifact and only extends for the first data point. The dip from 30 nm to 400 nm may also be an artifact, but it is also possible that a thin film of the blocking layer (undoped silicon) could remain as the sample surface and be sensed in the SIMS measurement. An integral under the SIMS curve from 30 nm to 15 $\mu$m yields an effective arsenic fluence of $\int_{30\,\mathrm{nm}}^{15\,\mu\mathrm{m}} N\mathrm{d}W = 1.42 \times 10^{15}\ \mathrm{cm}^{-2}$, where $N$ is the arsenic concentration and $W$ is the sputtered depth. In our initial analysis we will assume the transparent contacts are generally nonabsorbing and nonreflecting, but the FTS data will show this is probably not the case.

The photocurrent quantum yield data at a temperature of 12 K, supplied by the Rockwell Science Center [12], is reproduced in Fig. 3. Quantum yield is defined as the number of electrons produced per incident photon and equals the product of quantum efficiency and detector gain. The detectors show quantum yield near 0.6 in the range from 12 $\mu$m to

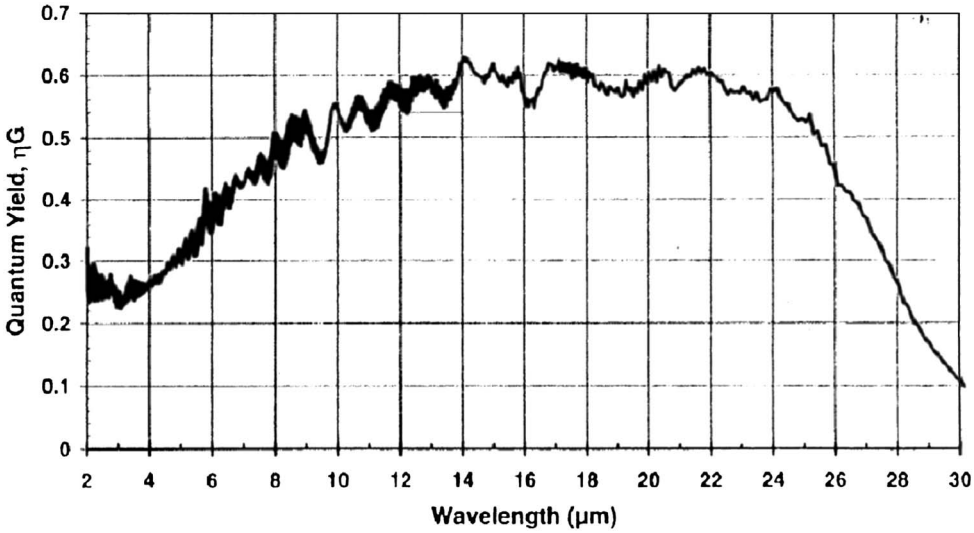


Fig. 3. Quantum yield data from calibrated photocurrent measurements on a BIB detector nominally identical to the device characterized optically in this study. Data supplied by Rockwell International, manufacturer of the BIB detectors [12].

24 $\mu$m with a gradual fall in quantum yield at shorter wavelengths and sharper cutoff in response at longer wavelengths. There is significant response (quantum yield >0.25) in the entire range from 4 $\mu$m to 28 $\mu$m. Significant spectral features are evident across the entire range of response, stemming from interference effects between reflections from the surfaces and thin film interfaces of the device. At least two different oscillation periods can be seen in the response, one with a short period that makes the data line appear thick (especially at short wavelengths) and another with a longer period evident as an envelope with multiple minima and maxima. Each type of oscillation extends its period at longer wavelengths, consistent with Fabry–Perot interference [13] between parallel surfaces. A major absorption feature from the silicon substrate can be seen near 16 $\mu$m.

The FTS data for transmittance and reflectance as a function of wavelength at room temperature and low temperature are presented in Fig. 4. As expected, there is increased absorption of the IR-AL at low temperature evident in both sets of data, with the largest change in transmittance between 4 $\mu$m and 30 $\mu$m. At room temperature most of the As donors are already thermally ionized, while below 20 K nearly no As donors are ionized and are thus nearly all available to absorb photons and be ionized. As with the photocurrent data, there are spectral oscillations in the transmittance and reflectance with at least two separate periods. Considering the short wavelength transmission data in Fig. 4, it can be seen that the amplitude of the short period oscillation increases significantly and the amplitude of the long period oscillation decreases significantly at low temperatures. The reason for the significant mismatch between the short and long wavelength cold transmittance data could not be determined, but in the analysis that follows, the mismatch will not affect the validity of the conclusions. The scale of the short wavelength data is considered more reliable, however, as the signal to noise for this dataset was superior, and in the calculations of processed data (e.g., optical parameters, absorptance and absorption cross section) the long wavelength transmittance data was first scaled to match the short wavelength data in the spectral range of overlap.

The nature of these oscillations can be more easily understood by considering the transmittance and reflectance as a function of wavenumber. Figure 5 displays the cold short wavelength data as a function of wavenumber, and it can be seen that there are two oscillation periods that are uniform across the entire wavenumber range. The short period oscillation, seen most easily in the transmittance data, is about 4 $\mathrm{cm}^{-1}$ (the resolution of the data), and the long period oscillation, evident in both the transmittance and the reflectance data, is approximately 95 $\mathrm{cm}^{-1}$. For Fabry–Perot interference, one expects (for normal incidence) a wavenumber separation between nearest transmission peaks of $1/(2dn)$, where $d$ is the separation of the surfaces and $n$ is their index of refraction. Etalon between the silicon surfaces of the detector and between the Si:As surfaces can explain these two distinct-period oscillations. Using values of $n = 3.42$ and $d = 350\ \mu$m for the silicon surfaces one calculates an oscillation period of 4.18 $\mathrm{cm}^{-1}$, in good agreement with the short period oscillation. Using $n = 3.42$ for the Si:As (assuming it has an index of refraction similar to silicon) and $d = 15\ \mu$m, the oscillation period calculated is 97.5 $\mathrm{cm}^{-1}$, in good agreement with the long period oscillation. As the resolution of the transmission data is very close to the period of the short oscillation, a distinctive envelope structure is evident around the 4 $\mathrm{cm}^{-1}$ oscillations, caused by incommensurability between the data sampling and oscillation period.

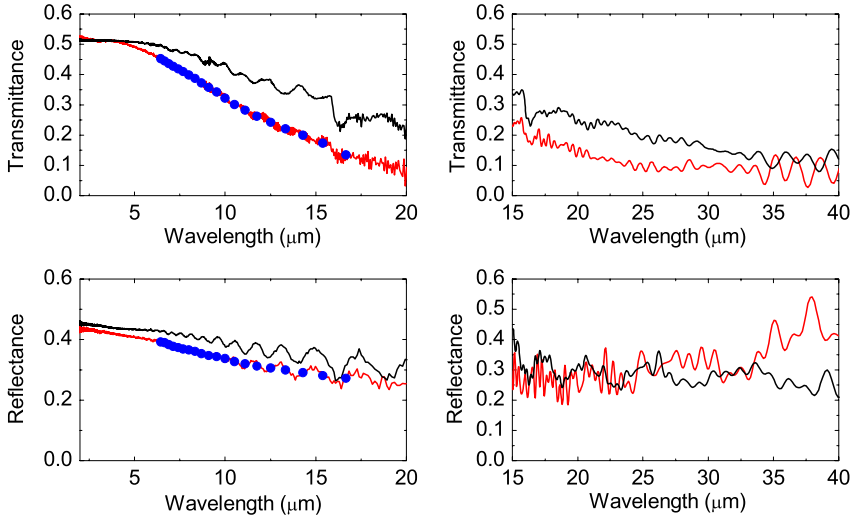


Fig. 4. (Color online) Transmittance and reflectance data for a deprocessed detector at room temperature (black) and low temperature (red). The transmittance data for short and long wavelength ranges are shown at the top, and the reflectance data in the bottom two graphs. Estimates of the incoherent limits of the transmittance and reflectance from the data are represented by the blue datapoints.

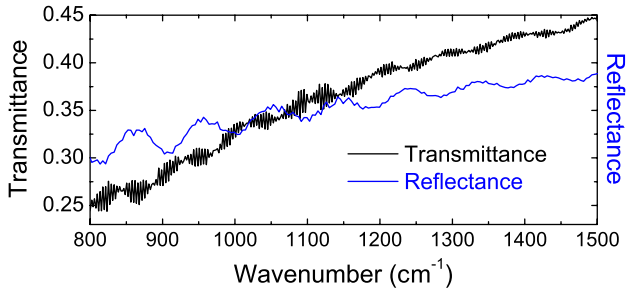


Fig. 5. (Color online) Cold transmittance and reflectance data over a limited wavenumber range, showing two clear oscillation periods, one of about 4 $cm^{-1}$ and the other about 95 $cm^{-1}$.

## 4. Analysis Procedures

Optical constants, as well as the low temperature absorption cross section of As in Si and the projected absorptance of the BIB devices can be calculated from the measured transmittance and reflectance. First a simple model will be used to calculate the absorption coefficient and reflectance of the arsenic-doped silicon, as well as estimates for its propagation constants $n$ and $k$. A more accurate model will then be introduced that can be used to refine the values of all the optical parameters for the Si:As. The optical parameters determined are effective values because etalon effects and multiple layers other than the AL complicate the determination of its properties. Etalon effects are small at the shorter wavelengths but can become a significant fraction of measured and calculated values at longer wavelengths. For instance, by 16 $\mu$m the etalon peaks reach 6.65% of the measured transmittance and 8.62% of the measured reflectance. At 16 $\mu$m these peaks in the transmittance and reflectance data lead to peaks in the calculated optical parameters between approximately 8% and 12% of their calculated values.

In the simplest model of the sample measured by FTS, one can assume that the properties of Si:As are similar enough to undoped silicon that there is negligible reflectance between the Si:As AL and the silicon substrate. Reflectance will be dominated by differences in the index of refraction, and as a zeroth order approximation it will be assumed that the Si:As and silicon have similar values for $n$. A schematic of the zeroth order model of the sample is shown in Fig. 6(a). The front surface of the sample is the AL and has an intensity reflectance $R_{\mathrm{AL}}^{\mathrm{air}}$, with transmission through the surface of $T_{\mathrm{AL}}^{\mathrm{air}} = 1 - R_{\mathrm{AL}}^{\mathrm{air}}$. The transmissivity $\xi_{\mathrm{AL}}$ through the AL is defined as $\xi_{\mathrm{AL}} = \exp(-\alpha_{\mathrm{AL}} W_{\mathrm{AL}})$, where $\alpha_{\mathrm{AL}}$ is the absorption coefficient of the AL and $W_{\mathrm{AL}}$ is its width. In this simplest approximation, it is assumed that there is no reflectance at the undoped silicon interface with the AL. The transmissivity through the silicon is $\xi_{\mathrm{Si}}$ and the reflectance at its back surface is $R_{\mathrm{Si}}^{\mathrm{air}}$; they are approximated using tabulated values of $n$ and $k$ for Si [14]. The transmission through the back surface is $T_{\mathrm{Si}}^{\mathrm{air}} = 1 - R_{\mathrm{Si}}^{\mathrm{air}}$. Let $\xi_{\mathrm{tot}} = \xi_{\mathrm{AL}} \cdot \xi_{\mathrm{Si}}$ be the

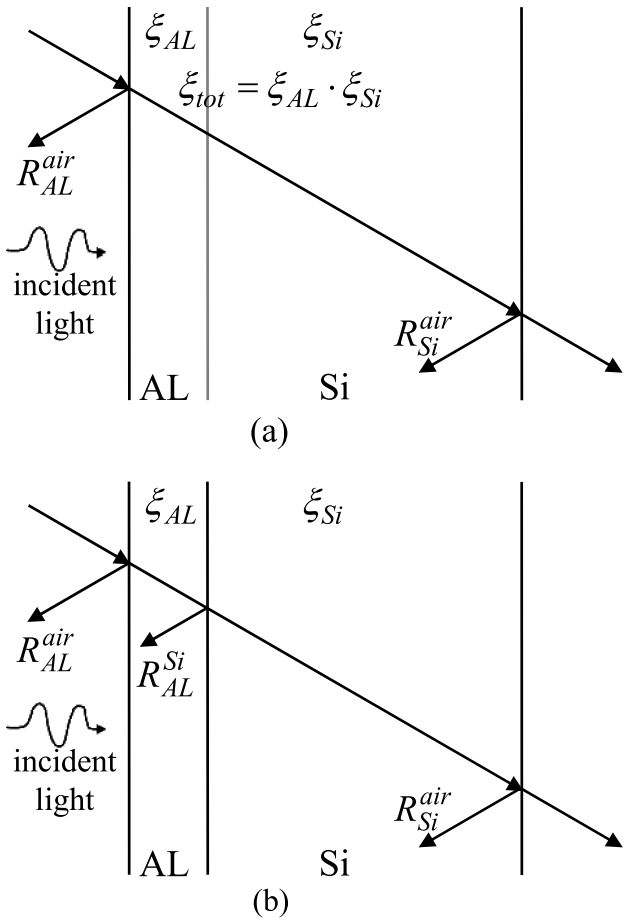


Fig. 6. (a) Schematic used in zeroth order calculations on the FTS data, where reflectance between Si:As and Si is considered negligible. It is assumed there is no absorption at the interfaces; (b) Schematic used in first order calculations on the FTS data, allowing for nonzero reflectance $R_{\mathrm{AL}}^{\mathrm{Si}}$.

transmissivity of the entire sample. It is assumed that the transparent contact is 100% transmitting.

Considering the infinite possible reflections between the front and back surfaces, one can determine the following expressions for the transmittance, reflectance, and absorptance of the sample in the incoherent approximation:

$$T_{\mathrm{tot}}^{(0)} = \xi_{\mathrm{tot}}(1 - R_{\mathrm{AL}}^{\mathrm{air}})(1 - R_{\mathrm{Si}}^{\mathrm{air}}) \frac{1}{1 - \xi_{\mathrm{tot}}^2 R_{\mathrm{AL}}^{\mathrm{air}} R_{\mathrm{Si}}^{\mathrm{air}}}$$

$$R_{\mathrm{tot}}^{(0)} = R_{\mathrm{AL}}^{\mathrm{air}} + \xi_{\mathrm{tot}}^2 (1 - R_{\mathrm{AL}}^{\mathrm{air}})^2 R_{\mathrm{Si}}^{\mathrm{air}} \frac{1}{1 - \xi_{\mathrm{tot}}^2 R_{\mathrm{AL}}^{\mathrm{air}} R_{\mathrm{Si}}^{\mathrm{air}}}$$

$$D_{\mathrm{tot}}^{(0)} = (1 - R_{\mathrm{AL}}^{\mathrm{air}})(1 - \xi_{\mathrm{tot}})(1 + R_{\mathrm{Si}}^{\mathrm{air}} \xi_{\mathrm{tot}}) \times \frac{1}{1 - \xi_{\mathrm{tot}}^2 R_{\mathrm{AL}}^{\mathrm{air}} R_{\mathrm{Si}}^{\mathrm{air}}}. \quad (1)$$

The expressions for transmittance and reflectance in Eq. (1) can be solved for $\xi_{\mathrm{tot}}$ and $R_{\mathrm{AL}}^{\mathrm{air}}$. This inversion process yields the following expressions for the transmissivity of the sample and the reflectance of the AL surface:

$$\xi_{\mathrm{tot}} = \frac{(R_{\mathrm{tot}}^{(0)} - 1)(1 - R_{\mathrm{Si}}^{\mathrm{air}}) + [(R_{\mathrm{tot}}^{(0)} - 1)^2(1 - R_{\mathrm{Si}}^{\mathrm{air}})^2 + 4(T_{\mathrm{tot}}^{(0)})^2 R_{\mathrm{Si}}^{\mathrm{air}}]^{1/2}}{2T_{\mathrm{tot}}^{(0)} R_{\mathrm{Si}}^{\mathrm{air}}} \qquad R_{\mathrm{AL}}^{\mathrm{air}} = \frac{T_{\mathrm{tot}}^{(0)} - \xi_{\mathrm{tot}}(1 - R_{\mathrm{Si}}^{\mathrm{air}})}{\xi_{\mathrm{tot}}[T_{\mathrm{tot}}^{(0)} \xi_{\mathrm{tot}} R_{\mathrm{Si}}^{\mathrm{air}} - (1 - R_{\mathrm{Si}}^{\mathrm{air}})]}. \quad (2)$$

The transmissivity, absorption coefficient, absorptance and absorption cross section of the IR-AL are then

$$\begin{aligned}
\xi_{\mathrm{AL}} &= \frac{\xi_{\mathrm{tot}}}{\xi_{\mathrm{Si}}} \\
\alpha_{\mathrm{AL}} &= -\frac{\ln(\xi_{\mathrm{AL}})}{W_{\mathrm{AL}}} \\
D_{\mathrm{AL}}^{(0)} &= (1 - R_{\mathrm{AL}}^{\mathrm{air}})(1 - \xi_{\mathrm{AL}})(1 + R_{\mathrm{Si}}^{\mathrm{air}} \xi_{\mathrm{AL}}) \\
&\quad \times \frac{1}{1 - \xi_{\mathrm{AL}}^2 R_{\mathrm{AL}}^{\mathrm{air}} R_{\mathrm{Si}}^{\mathrm{air}}} \\
\sigma_{\mathrm{AL}} &= \frac{\alpha_{\mathrm{AL}}}{N} = \frac{-\ln(\xi_{\mathrm{AL}})}{N W_{\mathrm{AL}}} = \frac{-\ln(\xi_{\mathrm{AL}})}{\int_0^{W_{\mathrm{AL}}} N \mathrm{d}W},
\end{aligned} \quad (3)$$

where $W_{\mathrm{AL}}$ is the width of the AL and $N$ is arsenic concentration of the AL.

Estimates for effective $k_{\mathrm{AL}}$ and $n_{\mathrm{AL}}$ can be made from the values for $\xi_{\mathrm{AL}}$ and $R_{\mathrm{AL}}^{\mathrm{air}}$ calculated from the data. The propagation constants are related to $\xi_{\mathrm{AL}}$ and $R_{\mathrm{AL}}^{\mathrm{air}}$ through the following expressions:

$$\begin{aligned}
k_{\mathrm{AL}} &= -\frac{\lambda}{4\pi W_{\mathrm{AL}}} \ln(\xi_{\mathrm{AL}}) \\
n_{\mathrm{AL}} &= \frac{-(R_{\mathrm{AL}}^{\mathrm{air}} + 1) - [(R_{\mathrm{AL}}^{\mathrm{air}} + 1)^2 - (1 + k_{\mathrm{AL}}^2)(R_{\mathrm{AL}}^{\mathrm{air}} - 1)^2]^{1/2}}{(R_{\mathrm{AL}}^{\mathrm{air}} - 1)}.
\end{aligned} \quad (4)$$

With the estimates for $n_{\mathrm{AL}}$ and $k_{\mathrm{AL}}$, a value for the reflectance between the IR-AL and the silicon substrate can be computed, and this value can be used to make more accurate estimates for the optical parameters of the sample. The reflectance between the AL and silicon can be found from $R_{\mathrm{AL}}^{\mathrm{Si}} = [(n_{\mathrm{Si}} - n_{\mathrm{AL}})^2 + (k_{\mathrm{Si}} - k_{\mathrm{AL}})^2]/[(n_{\mathrm{Si}} + n_{\mathrm{AL}})^2 + (k_{\mathrm{Si}} + k_{\mathrm{AL}})^2]$.

A more accurate model for the sample than has thus far been used would allow for a nonzero reflectance between the AL and silicon and this configuration is shown in the schematic of Fig. 6(b). For this more complete first order model, expressions for $T_{\mathrm{tot}}$, $R_{\mathrm{tot}}$, and $D_{\mathrm{tot}}$ can be derived similar to those found in Equations 1. These expressions can be inverted and yield equations similar to Eq. (2), providing more accurate estimates for $\xi_{\mathrm{AL}}$ and $R_{\mathrm{AL}}^{\mathrm{air}}$, and then for $n_{\mathrm{AL}}$ and $k_{\mathrm{AL}}$ from Eq. (4). One could calculate the pair $(\xi_{\mathrm{AL}}, R_{\mathrm{AL}}^{\mathrm{air}})$ from the data and an initial estimate for $R_{\mathrm{AL}}^{\mathrm{Si}}$, and then iteratively find a refined value of $R_{\mathrm{AL}}^{\mathrm{Si}}$ from the pair $(\xi_{\mathrm{AL}}, R_{\mathrm{AL}}^{\mathrm{air}})$ and then new estimates of $(\xi_{\mathrm{AL}}, R_{\mathrm{AL}}^{\mathrm{air}})$ from the refined $R_{\mathrm{AL}}^{\mathrm{Si}}$, ending the procedure when the values for $R_{\mathrm{AL}}^{\mathrm{Si}}$ converge.

In this work, we will only make use of the first order expression for the absorptance $D_{\mathrm{tot}}$, which can be used to compare the estimated detector AL absorptance with the quantum yield from the photocurrent data. This expression is calculated for the full detector configuration, which can be approximately represented by the schematic in Fig. 7. The first order expression for absorptance $D_{\mathrm{tot}}$ is given by

$$\begin{aligned}
D_{\mathrm{tot}} &= (1 - R_{\mathrm{Si}}^{\mathrm{air}}) \frac{1}{1 - \xi_{\mathrm{Si}}^2 R_{\mathrm{sub}} R_{\mathrm{Si}}^{\mathrm{air}}} [(1 - \xi_{\mathrm{Si}}) \\
&\quad \times (1 + R_{\mathrm{sub}} \xi_{\mathrm{Si}}) + \xi_{\mathrm{Si}} D_{\mathrm{sub}}] \\
\text{where } R_{\mathrm{sub}} &= R_{\mathrm{AL}}^{\mathrm{Si}} + \xi_{\mathrm{AL}}^2 (1 - R_{\mathrm{AL}}^{\mathrm{Si}})^2 \\
&\quad \times R_{\mathrm{metal}} \frac{1}{1 - \xi_{\mathrm{AL}}^2 R_{\mathrm{AL}}^{\mathrm{Si}} R_{\mathrm{metal}}} \\
\text{and} \quad D_{\mathrm{sub}} &= (1 - R_{\mathrm{AL}}^{\mathrm{Si}})(1 - \xi_{\mathrm{AL}})(1 + R_{\mathrm{metal}} \xi_{\mathrm{AL}}) \\
&\quad \times \frac{1}{1 - \xi_{\mathrm{AL}}^2 R_{\mathrm{AL}}^{\mathrm{Si}} R_{\mathrm{metal}}},
\end{aligned} \quad (5)$$

where $R_{\mathrm{metal}}$ is the reflectance of aluminum, assumed to be 98% across the spectral range measured. The term including $D_{\mathrm{sub}}$ in the expression for $D_{\mathrm{tot}}$ in Eq. (5) represents the absorption in the AL alone, so the separate contributions to the absorptance of substrate and AL can be estimated. For $R_{\mathrm{AL}}^{\mathrm{Si}} \ll 1$, one can approximate:

$$\begin{aligned}
D_{\mathrm{AL}} &\approx \xi_{\mathrm{Si}}(1 - R_{\mathrm{Si}}^{\mathrm{air}})(1 - R_{\mathrm{AL}}^{\mathrm{Si}})(1 - \xi_{\mathrm{AL}}) \\
&\quad \times (1 + R_{\mathrm{metal}} \xi_{\mathrm{AL}}) \frac{1}{1 - \xi_{\mathrm{Si}}^2 \xi_{\mathrm{AL}}^2 R_{\mathrm{Si}}^{\mathrm{air}} R_{\mathrm{metal}}}.
\end{aligned} \quad (6)$$

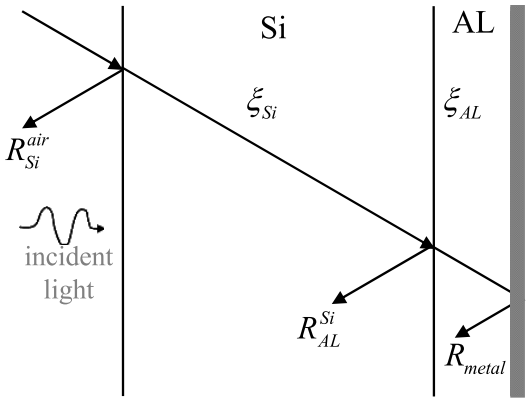


Fig. 7. Schematic used in the calculations of the cross section and estimated absorptance for the full BIB detector. The shaded layer on the right side of the figure is the aluminum high reflectance layer used to boost detector absorption.

The absorptance in Eq. (6) gives an upper limit for the detector quantum efficiency, and the ratio of the quantum efficiency to the absorptance could be considered the collection efficiency, as long as absorption unrelated to donor photo-ionization is minimal.

### 5. Analysis Results and Discussion

Simple estimates of the transmittance and reflectance of the sample in the absence of etalon effects can be made. For transmittance, Eq. (1) is modified in the case of coherence effects to be

$$T_{\mathrm{tot}}^{(\delta)} = \xi_{\mathrm{tot}}(1-R_{\mathrm{AL}}^{\mathrm{air}})(1-R_{\mathrm{Si}}^{\mathrm{air}}) \times \frac{1}{1+\xi_{\mathrm{tot}}^2 R_{\mathrm{AL}}^{\mathrm{air}} R_{\mathrm{Si}}^{\mathrm{air}} - \left(2\xi_{\mathrm{tot}}\sqrt{R_{\mathrm{AL}}^{\mathrm{air}} R_{\mathrm{Si}}^{\mathrm{air}}}\right)\cos\delta}, \quad (7)$$

where $\delta$ is the phase associated with the electric field of the light incident on the sample. It can be noted that $T_{\mathrm{tot}}^{(0)} = \sqrt{T_{\mathrm{tot}}^{(\delta=0)} T_{\mathrm{tot}}^{(\delta=\pi)}}$ from Eqs. (1) and (8); thus the geometric mean of the maximum and minimum values (etalon peaks) in the data provide an estimate of the incoherent expression. For reflectance, in the case where $R_{\mathrm{AL}}^{\mathrm{air}} \approx R_{\mathrm{Si}}^{\mathrm{air}}$, Eq. (1) is modified in the case of coherence effects to be (replacing both $R_{\mathrm{AL}}^{\mathrm{air}}$ and $R_{\mathrm{Si}}^{\mathrm{air}}$ by $R$)

$$R_{\mathrm{tot}}^{(\delta)} = R + \xi_{\mathrm{tot}}(1-R)R\frac{\xi_{\mathrm{tot}}(1+R) - 2\cos\delta}{1-\xi_{\mathrm{tot}}^2 R^2 - 2\xi_{\mathrm{tot}} R\cos\delta}. \quad (8)$$

It can be noted that $R_{\mathrm{tot}}^{(0)} = R_{\mathrm{tot}}^{(\delta=\arccos(\xi R))}$, so that at specific wavenumber values the coherent and incoherent expressions agree. Using these relationships regarding transmittance and reflectance, estimates of their incoherent limits were made from the data, and these estimates are plotted using circular datapoints in Fig. 4 over the range from approximately 6.5 $\mu$m to 16.7 $\mu$m (1550 cm$^{-1}$ to 600 cm$^{-1}$).

The calculated zeroth order values for the transmissivity $\xi_{\mathrm{AL}}$ and reflectance $R_{\mathrm{AL}}^{\mathrm{air}}$ using Eq. (2) are shown in Fig. 8; the estimates for effective $n_{\mathrm{AL}}$ and $k_{\mathrm{AL}}$ using Eq. (4) are shown in Fig. 9. Values for $R_{\mathrm{AL}}^{\mathrm{air}}$ and $n_{\mathrm{AL}}$ are similar to those for silicon, but $k_{\mathrm{AL}}$ ($\xi_{\mathrm{AL}}$) is significantly enhanced (reduced) from silicon over nearly all the spectral range measured. Estimates of these calculated optical parameters in the incoherent limit from the transmittance and reflectance data are represented by circular datapoints in Figs. 8 and 9. The value for the low temperature absorption cross section of arsenic in silicon (for As concentration of $10^{18}$ cm$^{-3}$) is shown in Fig. 10 and is compared with data from Geist for Si:As with As concentration $8.4 \times 10^{17}$ cm$^{-3}$ [11]. There is excellent agreement in the curves down to 500 cm$^{-1}$, but at the lowest wavenumbers, the value computed for the cross section does not decline as would be expected for Si:As, and as seen in Geist's data. A possible explanation for this is that the buried "transparent" contact in

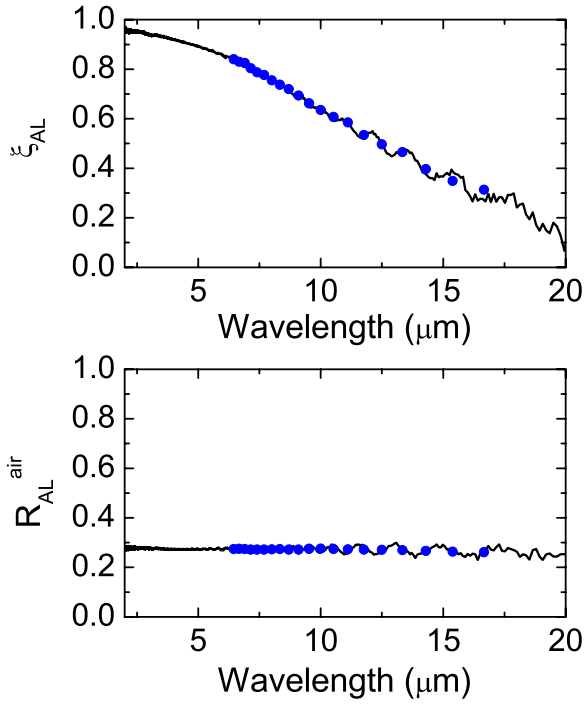


Fig. 8. (Color online) Calculated values for transmissivity $\xi_{\mathrm{AL}}$ (top) and reflectance $R_{\mathrm{AL}}^{\mathrm{air}}$ (bottom). Estimates of the incoherent limits of $\xi_{\mathrm{AL}}$ and $R_{\mathrm{AL}}^{\mathrm{air}}$ from the data are represented by the blue datapoints.

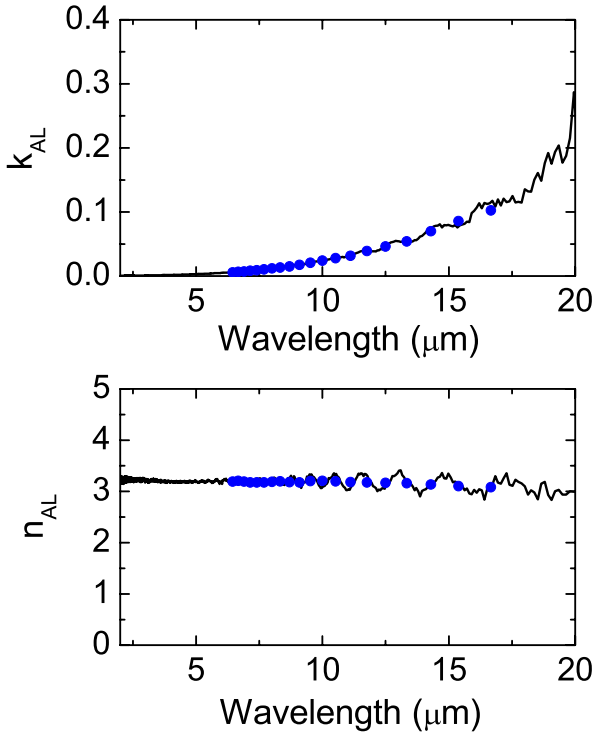


Fig. 9. (Color online) Calculated values for the propagation constants $k_{\mathrm{AL}}$ (top) and $n_{\mathrm{AL}}$ (bottom). The data has not been smoothed, so the significant spectral oscillations associated with etalon seen in the raw data are also evident in these calculated values. Estimates of the incoherent limits of $k_{\mathrm{AL}}$ and $n_{\mathrm{AL}}$ from the data are represented by the blue datapoints.

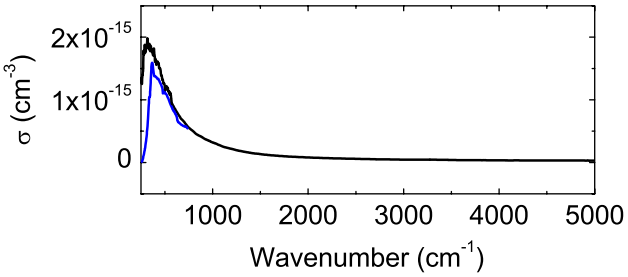


Fig. 10. (Color online) Comparison of absorption cross section for As in Si published by Geist (blue) and determined in this study from the FTS measurements (black).

our samples is not truly nonreflecting and nonabsorbing at low wavenumbers, lowering the transmission and raising the calculated absorption cross section in this range. The possibility that such a contact is not highly transparent at long wavelengths has been mentioned previously by Petroff and Stapelbroek; such a contact exhibits free carrier absorption and as designed may already exhibit 15% absorption at 25 $\mu$m, but nonoptimum contacts may show as little as 25% transmission at 20 $\mu$m [15].

More evidence that the AL becomes transmissive at long wavelengths but the contact layer does not can be seen in the cold data of Fig. 4. Beyond 25 $\mu$m, both the amplitude of the long period oscillation in the reflectance and the average value of reflectance appear to increase markedly. The long period oscillation is associated with the thin AL and an increase in its amplitude would be consistent with the AL becoming less absorbent. An increase in reflectance would be consistent with both an increase in the reflectance of the buried contact and a decrease in the absorption of the AL. Unlike the reflectance, the average transmission shows little change beyond 25 $\mu$m, consistent with the buried contact continuing to block transmission, even when the AL becomes less absorbent. The agreement in shape with the Geist data for wavelengths below 20 $\mu$m indicates that any spectral skewing of results of the calculated parameters for the AL by a nonideal transparent contact may be limited to the range beyond 20 $\mu$m (less than 500 $\mathrm{cm}^{-1}$).

The absorptance of the detector from the FTS data has been calculated using the models and analysis described in the Analysis Procedures section and verified by determining the absorptance using several different methods. Three types of calculations were made and compared, and they all yielded nearly identical results. First, the simple zeroth order calculation was made and used to estimate the absorptance $D_{\mathrm{tot}}^{(0)}$ [from Eq. (1)] of the detector configuration in Fig. 7 (with $R_{\mathrm{AL}}^{\mathrm{Si}} = 0$). Second, the full iterative first order treatment described in the Analysis Procedures section was carried out until $R_{\mathrm{AL}}^{\mathrm{Si}}$ converged. The absorptance $D_{\mathrm{tot}}$ [from Eq. (5)] for the detector configuration from this calculation agreed with $D_{\mathrm{tot}}^{(0)}$ from the zeroth order calculation. Also, the calculated value for the $D_{\mathrm{sub}}$ term of $D_{\mathrm{tot}}$ in Eq. (5) was compared to the absorptance calculated from Eq. (6) using the first order results and these values were nearly identical, indicating Eq. (6) is a good approximation. Third, a coherent model for the detector configuration with three layers (silicon, AL, and aluminum) was developed using $n$ and $k$ from the literature for silicon and aluminum and propagation constants for the AL from our zeroth order calculations. The model was averaged over incident angle and polarization and then appropriately averaged to account for the wavenumber resolution of the measured data. The absorptance of the detector configuration calculated from this model agreed well with the zeroth and first order incoherent calculations with some deviation at wavelengths shorter than 8 $\mu$m (possibly due to the more detailed description of the aluminum properties in the coherent model). The agreement between incoherent and coherent results implies that the incoherent model is a valid approximation for the system under study.

The estimated AL absorptance for the detector was calculated from the FTS data using Eq. (6) and is compared in Fig. 11 to the quantum yield calculated from the photocurrent data. As discussed in the Analysis Procedures section, the AL absorptance can be related to the detector quantum efficiency by an effective collection efficiency, i.e., $\mathrm{QE} = \mathrm{CE} \times D_{\mathrm{AL}}$, where QE is the quantum efficiency (fraction of incident photons that are sensed by photodetection) and CE is the collection efficiency. The effective collection efficiency will be reduced, for instance, by recombination of low mobility carriers which do not reach the electrodes. The quantum yield, on the other hand, is related to the detector quantum efficiency by detector gain, i.e., $\mathrm{QY} = \mathrm{QE} \times G$, where QY is quantum yield and $G$ is detector gain. Gain will be increased above unity, for instance, by impact ionization related to high energy photons or large bias voltages. The ratio of quantum yield to AL absorptance, nominally equal to the product of collection efficiency and detector gain (i.e., $\mathrm{QY}/D_{\mathrm{AL}} = \mathrm{CE} \times G$), is displayed in the inset of Fig. 11. This ratio is near one over the range from 10 $\mu$m to 25 $\mu$m, but rises significantly at shorter wavelengths and falls at longer wavelengths.

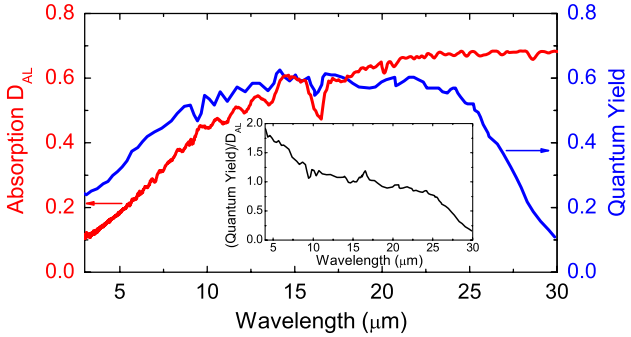


Fig. 11. (Color online) Comparison of AL absorptance determined from FTS optical measurements (red) and quantum yield determined from photocurrent (blue) measurements. The ratio of quantum yield to AL absorptance, which is approximately the product of collection efficiency and detector gain, is presented in the inset.

Fano impact ionization, which is known to be significant in BIB detectors at short wavelengths, raises the gain of the detector and could explain the behavior of the QY-to-absorptance ratio at short wavelengths. At long wavelengths, there are two potential explanations for the curve falling. The first possibility, already discussed in the absorption cross-section results, is that the buried contact may be significantly absorbing at long wavelengths. In the photoelectric measurement configuration, this will have the effect of filtering out photons before they reach the AL and thus will lower the quantum yield. In the FTS measurement configuration, the high absorption of the contact will raise the apparent absorption of the detector. Thus, an absorbing contact will lower the calculated QY-to-absorptance ratio. A second possibility is that impurity band carriers generated by relatively low energy photons are less mobile than those generated by high energy photons and have significantly higher chance of recombination before reaching the electrode [16]. In this case, collection efficiency, and thus the QY-to-absorptance ratio, would be reduced at long wavelengths.

The uncertainties in our measured transmittance and reflectance data are estimated to be approximately $\pm 2\%$ (coverage factor $k = 1$), and simple estimates for upper limits on uncertainty in our calculated values can be made assuming these uncertainties in the measured data. The full span of possible values for a calculated parameter was determined by allowing transmittance and reflectance inputs to range over all values within their uncertainty ranges. The percentage uncertainty associated with transmissivity $\xi_{AL}$ increases with increasing wavelength, and the percentage uncertainties associated with all other calculated values ($R_{AL}^{air}$, $k_{AL}$, $n_{AL}$, $D_{AL}$ and $\sigma$) decrease with increasing wavelength. Over the range from $2\,\mu$m to $20\,\mu$m, the maximum uncertainty associated with $\xi_{AL}$ is about $\pm 2.8\%$, and its uncertainty at $10\,\mu$m is approximately $\pm 2.4\%$. At $2\,\mu$m, the maximum uncertainties associated with $R_{AL}^{air}$ and $n_{AL}$ are $\pm 15\%$ and $\pm 11\%$, respectively. The uncertainties for $R_{AL}^{air}$ and $n_{AL}$ fall slowly with increasing wavelength and at $10\,\mu$m are $\pm 14\%$ and $\pm 10\%$, respectively. The uncertainties for $k_{AL}$, $D_{AL}$, and $\sigma$ are all approximately $\pm 45\%$ at $2\,\mu$m but then fall quickly with increasing wavelength. At $10\,\mu$m, the estimated uncertainties for $k_{AL}$ and $\sigma$ are $\pm 6\%$ and the estimated uncertainty for $D_{AL}$ is $\pm 3\%$.

## 6. Conclusions

We have calculated effective values for the propagation constants, or alternatively the transmissivity $\xi_{AL}$ and reflectance $R_{AL}^{air}$, of Si:As at cryogenic temperatures over the spectral range $2\,\mu$m to $30\,\mu$m from spectral measurements of transmittance and reflectance on partially deprocessed BIB detectors. The methods developed for extraction of the propagation constants from transmittance and reflectance can be generally applied to layered detectors such as BIBs. These calculated optical constants have been used to estimate the absorption cross section of As in Si and the AL absorptance of a detector based on this material. The absorption cross section agrees well with previously published results for similar dopings of As in Si, indicating that our measurement results are reliable. For the detector absorptance estimates, a simple zeroth order incoherent calculation and an iterative first order incoherent method, allowing nonzero reflectance between detector substrate and AL, were developed and analyzed. Both methods yield nearly identical results, and the calculated value for $R_{AL}^{Si}$, the reflectance between the AL and silicon substrate, is below 2% over the spectral range. A coherent calculation of the detector absorptance agrees well with the detector absorptance from the incoherent calculations, implying that use of the incoherent approximation is valid for this experimental system. The AL absorptance results from our FTS measurements are compared to quantum yield results from photoelectric measurements.

It would be of value to repeat the FTS measurements made here on samples without the buried contact layer as this could yield a more accurate determination of the optical properties of the Si:As. This would potentially raise other problems in comparison with the photocurrent data, however, as the samples used for optical characterization would be less similar to the complete BIB devices. Spectral comparison between the FTS data and the photocurrent data could be significantly simplified all the same, especially at long wavelengths. Using the optical methods and analysis described, it is possible to predict AL absorptance of a BIB device before fabrication by measurement of the optical properties of the blanket films from which it will be composed. This data, along with complementary electronic measurements, can be used to assess and qualify detector growth material before beginning the device fabrication process.

The authors would like to thank Maryn "Dutch" Stapelbroek (University of Arizona), Jon Geist (NIST) and Henry Hogue (DRS) for very helpful discussions in developing a consistent interpretation of our data and for reviewing our manuscript.

## References and Notes

1. M. D. Petroff and M. G. Stapelbroek, "Blocked impurity band detectors," U.S. patent 4,568,960 (February 4, 1986).
2. R. D. Campbell, "Characterization of the Si:As blocked impurity band (BIB) detector in Keck's long wavelength spectrometer (LWS)," Exp. Astron. **14**, 57–60 (2002).
3. A. K. Mainzer, H. Hogue, M. Stapelbroek, D. Molyneux, J. Hong, M. Werner, M. Ressler, and E. Young, "Characterization of a megapixel mid-infrared array for high background applications," Proc. SPIE **7021**, 70210T-1–70210T-6 (2008).
4. B. L. Cardozo, E. E. Haller, L. A. Reichertz, and J. W. Beeman, "Far infrared absorption in GaAs: Te liquid phase epitaxial films," Appl. Phys. Lett. **83** (19), 3990–3992 (2003).
5. A. C. Carter, S. R. Lorentz, T. M. Jung, B. J. Klemme, and R. U. Datla, "NIST Facility for spectral calibration of

detectors: calibration of arsenic doped silicon blocked impurity band detectors," Proc. SPIE **4028**, 420–425 (2000).
6. T. M. Jung, A. C. Carter, S. R. Lorentz, and R. U. Datla, "NIST-BMDO Transfer Radiometer (BXR)," Proc. SPIE **4028**, 404–410 (2000).
7. A. C. Carter, S. I. Woods, S. M. Carr, T. M. Jung, and R. U. Datla, "Absolute cryogenic radiometer and solid state trap detectors for IR power scales down to 1 pW with 0.1% uncertainty," Metrologia **46** (4), S146–S150 (2009).
8. E. J. Iglesias, A. W. Smith, and S. G. Kaplan, "A sensitive, spatially uniform photodetector for broadband infrared spectrophotometry," Appl. Opt. **47** (13), 2430–2436 (2008).
9. M. D. Petroff and M. G. Stapelbroek, "Responsivity and noise models of blocked impurity band detectors. IRIA-IRIS," in *Proceedings of the Meeting of the Specialty Group on Infrared Detectors*, Volume 2 (ERIM, 1984).
10. F. Szmulowicz, F. L. Madarsz, and J. Diller, "Temperature dependence for the figures of merit for blocked impurity band detectors," J. Appl. Phys. **63** (11), 5583–5588 (1988).
11. J. Geist, "Infrared absorption cross section of arsenic in silicon in the impurity band region of concentration," Appl. Opt. **28**, 1193–1199 (1989).
12. Reference is made to commercial laboratories and products to adequately specify the experimental procedures involved. Such identification does not imply recommendation or endorsement by the National Institute of Standards and Technology, nor does it imply that these laboratories or products are the best for the purpose specified.
13. M. Born and E. Wolf, *Principles of Optics*, 5th ed. (Pergamon, 1975), pp. 323–329.
14. D. F. Edwards, "Silicon (Si)," in *Handbook of Optical Constants of Solids*, E. D. Palik, ed. (Academic, 1985) pp. 547–569.
15. M. D. Petroff and M. G. Stapelbroek, "Spectral response, gain, and noise models for IBC detectors," in *IRIA-IRIS, Proceedings of the Meeting of the Specialty Group on Infrared Detectors* (ERIM, 1985).
16. Jon Geist (NIST), private communication.